Stochastic Inverse Modeling and Global Sensitivity Analysis to Assist Interpretation of Drilling Mud Losses in Fractured Formations

A. Russian*(1), M. Riva(1,2), E. R. Russo(3), M. A. Chiaramonte(3), A. Guadagnini(1,2)

(1) Department of Civil and Environmental Engineering, Milano, Politecnico di Milano, Piazza Leonardo da Vinci 32, 20133, Milano, Italy

(2) Department of Hydrology and Atmospheric Sciences, University of Arizona, Tucson, AZ, 85721, USA

(3) Geolog Srl, via Monte Nero 30, 20098, San Giuliano Milanese, Milano, Italy

* Corresponding author, e-mail address: anna.russian@polimi.it, phone: +39 02 2399 6214

Keywords: Stochastic Calibration; Drilling Mud Losses; Parameter Uncertainty; Global Sensitivity Analysis; Fractured Formations.

Highlights:

- Stochastic Calibration and Global Sensitivity Analysis
- Analytical Model for Drilling Mud Losses Interpretation in Fractured Formations
- Comparison of Stochastic Calibration Methods

Abstract:

This study is keyed to enhancing our ability to characterize naturally fractured reservoirs through quantification of uncertainties associated with fracture permeability estimation. These uncertainties underpin the accurate design of well drilling completion in heterogeneous fractured systems. We rely on monitored temporal evolution of drilling mud losses to propose a non-invasive and quite inexpensive method to provide estimates of fracture aperture and fracture mud invasion together with the associated uncertainty. Drilling mud is modeled as a yield power law fluid, open fractures being treated as horizontal planes intersecting perpendicularly the wellbore. Quantities such as drilling fluid rheological properties, flow rates, pore and dynamic drilling fluid pressure, or wellbore geometry, are often measured and available for modeling purposes. Due to uncertainty associated with measurement accuracy and the marked space-time variability of the investigated phenomena, we ground our study within a stochastic framework. We discuss (*a*) advantages and drawbacks of diverse stochastic calibration strategies and (*b*) the way the posterior probability densities (conditional on data) of model parameters are affected by the choice of the inverse modeling approach employed. We propose to assist stochastic model calibration through results of a moment-based global sensitivity analysis (GSA). The latter enables us to investigate the way parameter uncertainty influences key statistical moments of model outputs and can contribute to alleviate computational costs. Our results suggest that combining moment-based GSA with stochastic model calibration can lead to significant improvements of fractured reservoir characterization and uncertainty quantification.

1. Introduction

Naturally fractured reservoirs (NFRs) play a prominent role in energy supply. These systems represent about 48% of oil reservoirs, with more than of 60% of oil and 40% of gas reserves being associated with fractured carbonate reservoirs (World Energy Outlook 2006), and are typically highly heterogeneous (Roehl and Choquette 1985), thus rendering the evaluation of their potential production a significantly challenging task. Reservoir characterization requires the evaluation of the spatial distribution of petrophysical parameters, such as permeability and porosity. This step is usually performed through an inverse modeling approach (Carrera and Neuman 1986, Carrera et al. 2005), making use of observations of available state variables (such as pressure and/or velocity distribution). In fractured reservoirs, open fractures govern hydrocarbon production and reservoir permeability. To date, no technology can provide real-time estimates of fractures permeability while drilling, this parameter being typically assessed by combining diverse technologies such as seismic, downhole image logs, magnetic resonance, core analysis and transient well testing. These technologies are very expensive and require an often long and high-priced downtime. Having at our disposal an efficient and relatively inexpensive approach to provide real time characterization of NFRs is key for a successful drilling campaign. Estimating fracture aperture and extent while drilling would optimize borehole logging by focusing solely on critical sections of the wellbore, thus contributing to saving of time and reducing costs. Moreover, a real time NFRs characterization would contribute to increase drilling efficiency by optimizing the lost circulation material plan and the non-productive time (Razavi et al. 2017).

Here, we propose a non-invasive and quite inexpensive method to provide (quasi) real-time estimates of fractures' aperture and extent while drilling. The approach is based on monitoring and analysis of the real-time evolution of drilling mud losses and makes use of a relatively simple analytical model. Mud is modeled as a yield power law fluid (Majidi et al. 2010) and fractures are treated as horizontal planes, perpendicular to the wellbore. Lavrov (2014) proposed a more complex model considering drilling mud flow into a deformable horizontal fracture of finite length, while Razavi et al. (2017)

72 incorporate leak-off phenomena into the formation matrix by modeling both radial and linear flow
73 within the fractures. Both of these models consider a fluid characterized by a simplified rheology,
74 mud being modeled as a pure power-law fluid (neglecting the effects of the yield stress) and as a
75 Bingham plastic fluid by Lavrov (2014) and Razavi et al. (2017), respectively. Considering the
76 sources of uncertainty characterizing the scenario, we prefer to rest on a simple conceptual and
77 geometrical model, as in Majidi et al. (2010), and parametrize mud as a yield power law fluid,
78 consistent with experimental evidence. The parameters needed for the implementation of such a fluid
79 behavior are usually measured and available. As stated above, since fracture and reservoir properties
80 are uncertain, we tackle the problem within a stochastic inversion framework.

81 Inverse problems are usually ill-posed (e.g., Keller 1976). Non-uniqueness of the solution may
82 arise because the number of parameters to estimate exceeds the number of available observations
83 and/or in cases where observations are not sensitive to the model parameters to be estimated. A series
84 of methodologies have been proposed to mitigate such ill-posedness of the inverse problem,
85 including, e.g., approaches based on reducing the number of unknown parameters (i.e., by making
86 use of the pilot points method, Alcolea et al. 2006), introducing prior information and/or
87 regularization/penalty terms (Medina and Carrera 1996), minimizing non-linearities in the model
88 equations (e.g., Neuman 1973, Carrera and Neuman 1986, Zhou et al. 2014), or resorting to surrogate
89 models to reduce the number of model parameters to be estimated and/or decrease computational
90 time (e.g., Sudret et al. 2017).

91 Here, we tackle model calibration within a stochastic framework (e.g., Laloy et al. 2013, Mara
92 et al. 2017 and references therein). In this context one does not look for a unique solution and
93 considers multiple possible solutions to provide predictions under uncertainty. The latter is quantified
94 in terms of the posterior distribution of the parameters, i.e., the probability distribution of parameters
95 conditional on available information. Inverse stochastic calibrations tend to be computationally very
96 expensive. We propose to make use of global sensitivity analysis, GSA, (e.g., Song et al. 2015,

97 Pianosi et al. 2016) as an important tool to assist stochastic inverse modeling and reduce
98 computational time.
99 GSA allows quantifying the influence of uncertain model parameters (and their combined
100 effect) on the variability of a model output via global metrics (e.g., Razavi and Gupta 2015). GSA
101 techniques grounded on diverse approaches, including derivative-based (e.g., Campolongo et al.
102 2007), variance-based (e.g., Sobol 1993, Sochala and Le Maître 2013) and regression-based (e.g.,
103 Sudret 2007) techniques, have been proposed. Recently, Dell'Oca et al. (2017) introduced a moment-
104 based GSA approach, that quantifies the relative contribution of each uncertain model parameter to
105 the model output probability density function, as described via its statistical moments. While GSA
106 has been successfully used to assist the development of groundwater flow and transport models (e.g.,
107 Ratto et al. 2001, Van Griensven et al. 2006, Tang and Zhuang 2009, Chen et al. 2018), an assessment
108 of the way GSA can be employed to assist the evaluation of the posterior pdf of model parameters
109 within a stochastic inverse modeling framework is still lacking. This is a major goal of this study.
110 The work is organized as follows. Section 2 presents the analytical model employed during
111 GSA and stochastic calibrations. Section 3 illustrates the showcase scenario and the available dataset.
112 We also discuss the inherent uncertainty of model parameters and perform detailed numerical
113 analyses to test the reliability of the assumptions underpinning the analytical model developed in
114 Section 2 for the target scenario. Section 4 illustrates the results of the GSA approaches employed.
115 The latter are then used in Section 5, which is devoted to stochastic inverse modeling. Main findings
116 and conclusions are summarized in Section 6.
117
118 **2. Analytical model**
119 We model mud losses into a fracture intersecting a well by considering radial flow taking place
120 between two parallel circular disks. Mud flow advancement in the fracture can be described through
121 the momentum equation

$$\rho \frac{d\boldsymbol{v}}{dt} = \rho \boldsymbol{g} - \nabla \cdot \bar{\boldsymbol{\sigma}} \qquad \text{with} \quad \bar{\boldsymbol{\sigma}} = p' \bar{\boldsymbol{I}} + \bar{\boldsymbol{\tau}}. \tag{1}$$

Here, ρ [ML^{-3}] and $\boldsymbol{v}$ [LT^{-1}] are mud density and velocity vector, respectively; $\boldsymbol{g}$ [LT^{-2}] is gravity vector; $\bar{\boldsymbol{\sigma}}$ [$MT^{-2}L^{-1}$] is the total stress tensor; p' [$MT^{-2}L^{-1}$] is pressure; $\bar{\boldsymbol{I}}$ [-] is the identity matrix; and $\bar{\boldsymbol{\tau}}$ [$MT^{-2}L^{-1}$] is the shear stress tensor. The entries τ_{ij} of $\bar{\boldsymbol{\tau}}$ are characterized through the Herschel-Bulkley (H-B) rheological model

$$\begin{cases} \tau_{ij} = \tau_Y + 2^m k \left|\gamma_{ij}\right|^m & \text{for } i \neq j \text{ and } \left|\gamma_{ij}\right| \geq 0 \\ \tau_{ij} = 0 & \text{for } i \neq j \end{cases} \tag{2}$$

where τ_Y [$MT^{-2}L^{-1}$] is the fluid yield stress, k [$MT^{m-2}L^{-1}$] is the consistency index, m [-] is an index characterizing the (power-law) fluid behavior, and γ_{ij} [T^{-1}] are the components of the shear strain rate tensor $\bar{\boldsymbol{\gamma}}$ defined in (A.2). Note that (2) reduces to the model describing a Bingham plastic fluid for m = 1 and a Newtonian fluid for m =1 and τ_Y = 0, k representing fluid viscosity in both cases. The drilling mud is usually characterized by a shear thinning behavior according to which viscosity decreases with increasing $\bar{\boldsymbol{\gamma}}$ (i.e., m < 1).

In the following we consider laminar radial flow and thus neglect the transverse (v_θ) and vertical (v_z) components of $\boldsymbol{v}$. We futher assume that (*i*) radial velocity variations are much larger across the fracture thickness than along the radial direction $\left(\frac{\partial v_r}{\partial r} \ll \frac{\partial v_r}{\partial z}\right)$ and (*ii*) viscous forces dominate over inertial forces. Pressure is hydrostatic under these conditions and the radial derivative of $p = p' + \rho g$ is given by (see Appendix A, (A.7))

$$\frac{\partial p}{\partial r} = -k \frac{\partial}{\partial z}\left[\left(\frac{\partial v_r}{\partial z}\right)^m\right]. \tag{3}$$

The yield stress included in the rheological model (2) leads to the occurrence of a plug flow region (where $\partial v_r/\partial z = 0$) for $|z| \leq z_p$. Figure 1 provides a qualitative depiction of a fluid velocity profile across the planar fracture when no-slip conditions are imposed at fracture walls, i.e., $v_r(z = \pm w/2) = 0$. The value of z_p can be determined as described in the following. Making use of (2) and (A.4), the shear stress components τ_{rz} is given by

$$\tau_{rz} = \tau_Y + k\,|\frac{\partial v_r}{\partial z}|^m. \quad (4)$$

Taking the derivative of (4) with respect to z and making use of (3) yields

$$\frac{\partial p}{\partial r} = \frac{\partial \tau_{rz}}{\partial z}. \quad (5)$$

Integrating (5) with respect to z and setting $\tau_{rz} = \tau_Y$ enables one to compute the width of the plug flow region, z_p, as

$$z_p = \frac{\tau_Y}{-\partial p/\partial r} \quad . \quad (6)$$

The radial component of the velocity vector can then be derived integrating (3) along the vertical direction as

$$v_r(z) = \begin{cases} \frac{1}{k^{\frac{1}{m}}}\left(\frac{m}{m+1}\right)\left(-\frac{\partial p}{\partial r}\right)^{\frac{1}{m}}\left[\left(\frac{w}{2}-z_p\right)^{\frac{1+m}{m}} - \left(z-z_p\right)^{\frac{1+m}{m}}\right] & \text{for } |z| \geq z_p \\ \frac{1}{k^{\frac{1}{m}}}\left(\frac{m}{m+1}\right)\left(-\frac{\partial p}{\partial r}\right)^{\frac{1}{m}}\left[\left(\frac{w}{2}-z_p\right)^{\frac{1+m}{m}}\right] & \text{for } |z| < z_p \end{cases} \quad . \quad (7)$$

The mud flow rate, Q, and the overpressure, $\Delta p = p_w - p_f$, p_w and p_f respectively being the dynamic mud pressure at the well and at the mud front (i.e., the formation fluid pressure), are evaluated in Appendix A according to (A.8) and (A.10), respectively. Finally, the temporal evolution of the drilling mud volume loss, V_m, can be computed as

$$V_m(t) = \pi w[r_f^2(t) - r_w^2]\,, \quad (8)$$

where r_w is the wellbore radius and r_f is the location of the mud front (evaluated from the center of wellbore). The rate of advancement of r_f is obtained starting from (A.10) and setting $Q = dV_m/dt$, as

$$\frac{dr_f}{dt} = \frac{\left[\frac{\Delta p}{k} - \left(\frac{2m+1}{m+1}\right)\left(\frac{2\tau_Y}{wk}\right)(r_f - r_w)\right]^{\frac{1}{m}}\left[(1-m)\left(\frac{w}{2}\right)\right]^{\frac{1}{m}}\left(\frac{m}{2m+1}\,\frac{w}{2}\right)}{r_f\left(r_f^{1-m} - r_w^{1-m}\right)^{\frac{1}{m}}} \quad . \quad (9)$$

In (9) we invoke a quasi-steady state approximation and assume that the drilling fluid invading the fracture is driven by a constant overpressure Δp.

3. Showcase scenario and uncertain model parameters

The analytical model illustrated in Section 2 is here applied to a set of drilling mud loss data collected in a fractured carbonate reservoir. In this Section we (*i*) present the available data, (*ii*) introduce and discuss the model parameters and their inherent uncertainty, and (*iii*) address the reliability of the assumptions underlying the model introduced in Section 2.

3.1 Drilling Mud Loss Data

The drilling mud circuit is a closed system that can be subdivided into two segments, respectively termed (*a*) flow-in (extending from the surface into the well) and (*b*) flow-out (encompassing the portion conveying the mud fluid from the well back to surface). In the setting we analyze, the mud flow-in, Q_{in}, is evaluated from pump strokes and pump efficiency according to

$$Q_{in} = \sum_{i=0}^{n} SPM_i \Delta s_i \eta_i \,, \tag{10}$$

where n is the number of pumps installed at the rig site, SPM_i is the number of strokes per unit time of the i-th pump, Δs_i its the volume of drilling fluid displaced/injected per stroke, and η_i indicates pump efficiency. The mud flow rate conveyed to the surface through the flow-out line, Q_{out}, is (typically) measured with an electromagnetic flow meter. We term as *delta flow* the quantity $\Delta Q = Q_{out} - Q_{in}$. Real time monitoring of ΔQ is critical to provide information about borehole stability, a decrease of such a quantity being a signature of losses potentially due to the occurrence of a fracture or of a set of fractures (e.g., Majidi and Miska 2011; Al-Adwani et al. 2012).

We ground our study on data from four drilling mud loss events recorded at four different depths (hereafter termed events 1-4; numbering of events corresponds to increasing depths) while drilling a single well in a carbonate reservoir. Measurements of ΔQ have been collected at a relatively high frequency, corresponding to a uniform time step Δt = 5 s. An example of the available data is depicted in Figure 2.

Figure 3 depicts the temporal evolution of ΔQ (black symbols) measured for all four events while drilling the borehole. Note that time along the horizontal axis of each panel of Figure 3 is set

190 to zero at the beginning of the temporal window considered, for ease of comparison. Figure 3 shows
191 that ΔQ first fluctuates around a constant mean, ΔQ_0, for each event, this pattern being followed by a
192 sharp increase of $|\Delta Q|$, which finally decreases with time. The pattern displayed in each of the
193 subplots of Figure 3 is consistent with the presence of a fractured zone encountered (or formed) during
194 drilling. The total mud volume lost, $V_m^*(t)$, is also depicted (red crosses in Figure 3) for all events.
195 Values of V_m^* are calculated by integrating the mud flow rate ($Q^* = |\Delta Q| - \Delta Q_0$) invading the
196 fractured system over time. Note that ΔQ_0 is the mean delta flow measured before the described sharp
197 increase of $|\Delta Q|$ and is related to the advancement of the perforation, i.e., to the drilling rate of
198 penetration, and/or to the properties of the formation. We evaluate ΔQ_0 by averaging ΔQ data across
199 a temporal window of 300 s before the sharp increase of $|\Delta Q|$. The largest mud volume loss is
200 associated with event 4 (i.e., with the deepest fracture; Figure 3d), this event being also characterized
201 by the longest duration.
202
203 **3.2 Uncertain Model Parameters**
204 Here, we consider all parameters embedded in the analytical model described in Section 2,
205 i.e., w, τ_y, k , m, Δp, and r_w, as independent random variables, each characterized by a uniform
206 probability density function (pdf). Considering this modeling choice rests on the idea of assigning
207 equal weight to each value of the parameter distribution. We note that considering different prior
208 distributions and/or embedding statistical correlation among uncertain parameter would not alter the
209 workflow and can constitute an element of interest for future studies.
210 Upper and lower bounds of the variability range of each parameter are listed in Table 1. Since
211 the fracture aperture, w, is typically unknown, we allow this quantity to vary over several orders of
212 magnitude (with mean equal to 5 mm and a coefficient of variation of about 57%). The rheological
213 parameters (τ_y, k, and m) have been estimated from viscometer analyses as

214 $$\tau_Y = 2\theta_{300} - \theta_{600}\,, \quad m = 3.3219 \log_{10} \frac{\theta_{600} - \tau_y}{\theta_{300} - \tau_y}\,, \quad k = \frac{\theta_{300} - \tau_y}{511^m}\,, \tag{11}$$

where θ_i are shear stress measurements obtained from rotating cylinder viscometers operating at i rotations per minute (API draft 2009, Rehm et al. 2012). We obtained τ_Y = 4.59 Pa, m = 0.55 and k = 0.757 Pa s^m. These parameters are affected by uncertainty due to measurement errors. We further note that these estimates are associated with laboratory conditions, which differ from those encountered in a reservoir setting. Uncertainty bounds of rheological fluid parameters listed in Table 1 are associated with coefficients of variation ranging from 5% to 10% and are consistent with the study of Russo et al. (2018). Finally, Δp and r_w have been monitored along the depth of the wellbore on a routine basis during drilling. Values of Δp have been assessed by taking into account the drilling mud equivalent circulating density, ECD, and the pore pressure at the fracture depth. The width of the uncertainty intervals set in Table 1 for Δp and r_w enables us to encompass the range of all values monitored in the field setting analyzed.

3.3 Analytical versus Numerical results

Here, we test the reliability of the assumptions underpinning the analytical model illustrated in Section 2 within the parameter space defined in Table 1 and considering the range of measured values of |ΔQ| illustrated in Figure 3. We do so by comparing the analytical results computed via (*i*) (7) for the radial velocity and (*ii*) (A.10) for the overpressure against their numerical counterparts computed via the finite element software COMSOL Multiphysics v5.2 under steady-state conditions. As boundary conditions, we set a constant flow-rate at the well (inlet), no-slip at fracture walls, and zero pressure at the outlet. The numerical algorithm allows for high flexibility in modeling diverse rheology behaviors through the introduction of an apparent viscosity, μ, thus enabling one to recast (4) as

$$\tau_{rz} = \mu \left|\frac{\partial v_r}{\partial z}\right| \quad \text{with} \quad \mu = \tau_Y \left|\frac{\partial v_r}{\partial z}\right|^{-1} + k \left|\frac{\partial v_r}{\partial z}\right|^{m-1} . \tag{12}$$

Numerical implementation of (12) can lead to unstable results at the interface between the plug and the shear region (i.e., at $z = z_p$). For this reason and following the procedure proposed by

Mitsoulis and Abdali (1993), we multiply the term $\tau_Y \left|\frac{\partial v_r}{\partial z}\right|^{-1}$ in (12) by the smoothing function $(1 - a\left|\frac{\partial v_r}{\partial z}\right|)$ with $a = 0.1$. A numerical analysis (details not shown) allows recognizing that the results are not significantly affected by the value of a employed (with $0.01 \leq a \leq 1.00$).

Figure 4 depicts vertical profiles, with $z_D = z/(w/2)$, of (numerical and analytical) dimensionless velocity, v_D, and overpressure, p_D,

$$v_D = \frac{v}{\overline{v}}, \quad p_D = \frac{\Delta p}{k\left(\frac{\overline{v}}{w}\right)^m}, \quad \text{with} \quad \overline{v} = \frac{Q}{2\pi r w} \tag{13}$$

at three selected dimensionless radial distances from the well, $r_D = r/w$, and for a given combination of model parameter values selected within the bounds listed in Table 1. Results of similar quality have been obtained varying the model parameters (not shown). Analytical and numerical results are virtually indistinguishable (relative differences between analytical and numerical profiles in Figure 4 are always less than 1%). These findings suggest that the assumptions underlying the analytical solution (see Appendix A for details) are not violated under the tested conditions. Results of similar quality have also been recently obtained by Faysal et al. (2019) through a three-dimensional steady-state Computational Fluid Dynamics (CFD) study performed relying on the computational suite ANSYS® Fluent® (Ansys Inc. 2009).

The computational cost related to the numerical solution of the flow problem depends on the choice of parameters' values, each simulation being associated (on average) with a cost of the order of 30 minutes on a 2.9-GHz Intel Core i5 processor. This heavy CPU time would have rendered the global sensitivity analysis (Section 4) and the stochastic calibration (Section 5) of the model remarkably demanding in terms of computational time. The results of the comparison illustrated above gives us confidence to rely on the analytical model presented in Section 2 for the purpose of our studies. We recall that this model is fully analytical for the evaluation of the velocity profile (7) and requires solving numerically (9) for the evaluation of the mud front advancement, r_f. The latter has been solved within the Matlab® environment, requiring negligible CPU time.

4. Sensitivity Analysis

Here we evaluate the impact of parameter uncertainty on model results, expressed in terms of mud volume loss. We do so by jointly using (*i*) the qualitative scatter plot analysis (Saltelli et al. 2008), (*ii*) the classical variance-based global sensitivity analysis, GSA, (Sobol 1993), and (*iii*) the moment-based GSA (Dell'Oca et al. 2017). The latter allows quantifying the impact of uncertain model parameters on the pdf of model outputs, as rendered by their statistical moments. All results illustrated here are based on the solution of (8) - (9). As shown by (9), the advancement of mud front does not depends on the six uncertain parameters listed in Table 1, being otherwise influenced by a set of five independent variables (i.e., w, τ_Y/k, $\Delta p/k$, m, and r_w). The latter are then considered for the sensitivity analysis. Considering Table 1, one can see that τ_Y/k and $\Delta p(z)/k$ can vary within the interval [8.306 - 4.533] s^{-m} and [4.886 - 2.778] $\times 10^6$ s^{-m}, respectively.

4.1 Scatter Plot Analysis

Scatter plot analyses provide qualitative insights on the influence of model parameters on given quantities of interest. Scatter plots are here constructed through a uniform discretization of the parameter space, resulting in a total of 6^5 sampling points. Figure 5 depicts scatterplots highlighting the dependence of the total volume loss, V_m, on each model parameter. The mud volume loss is primarily influenced by the fracture aperture, data clouds denoting a nearly-linear (on average) increasing trend with w. Otherwise, increasing values of m correspond to a nonlinear decrease of V_m. A mild sensitivity of the results to the overpressure term $\Delta p/k$ is shown, no particular trend being observed with respect to parameters τ_Y/k or r_w.

4.2 Sobol' Indices

The total variance of V_m, $V(V_m)$, can be decomposed (Sobol 1993) as $V(V_m) = \sum_{i=1}^{N} V_i + \sum_{1\le i<j\le N} V_{i,j} + \cdots + V_{1,\ldots,N}$, where $N = 5$ is the number of model parameters, V_i is the contribution to $V(V_m)$ due to the uncertainty of only parameter P_i, and $V_{1,\ldots,s}$ is the contribution to $V(V_m)$ due to the interaction among the subset of parameters $[P_1, \ldots, P_s]$, with $s \le N$.

For each uncertain parameter P_i (i.e., $P_i = w$, τ_Y/k, $\Delta p/k$, m, or r_w) we compute the first order, S_i, and the total, S_i^T, Sobol' indices defined as

$$S_i = \frac{V_i}{V(V_m)}, \quad S_i^T = S_i + \sum_j S_{i,j} + \sum_{j,k} S_{i,j,k} + \cdots + S_{i,\ldots,N} \quad \text{with} \quad S_{1,\ldots,s} = \frac{V_{1,\ldots,s}}{V(V_m)} \ . \tag{14}$$

We recall that while S_i describes the amount of the total variance $V(V_m)$ due only to parameter P_i, S_i^T quantifies the total contribution of parameter P_i to $V(V_m)$, taking also into account the interaction among P_i and all remaining parameters. Values of S_i and S_i^T depicted in Figures 6a and 6b, respectively, are virtually identical, indicating that there are no significant joint effects of parameter uncertainties on $V(V_m)$. Consistent with our results of Section 4.1, $S_w > S_m > S_{\Delta p/k}$, i.e., the fracture width is the parameter which most affects $V(V_m)$, followed by m and $\Delta p/k$ while $S_{\tau_Y/k} \approx S_{rw} \approx 0$, i.e., τ_Y/k and r_w do not significantly affect $V(V_m)$.

4.3 Moment-based Global Sensitivity Analysis

Dell'Oca et al. (2017) introduced moment-based sensitivity indices, termed as AMA indices, which enable us to quantify the way uncertain model parameters influence a given statistical moment, $M(V_m)$, of the model output V_m. The AMA indices are defined as:

$$\mathrm{AMA}M_i = \begin{cases} \frac{1}{|M(V_m)|} E[|M(V_m) - M[V_m|P_i]|] & \text{if } |M(V_m)| \neq 0 \\ E[|M[V_m|P_i]|] & \text{if } |M(V_m)| = 0 \end{cases} . \tag{15}$$

Here, $\mathrm{AMA}M_i$ corresponds to the AMA index associated with the statistical moment $M(V_m)$ (where $M = E$, V, S or K, indicates expected value, variance, skewness and kurtosis, respectively) and related to parameter P_i; $M[V_m|P_i]$ denotes the statistical moment M conditional to a known value of

parameter P_i. These indices quantify the expected distance between a given statistical moment of V_m conditional to values of a model parameter and its unconditional counterpart. Note that AMAV_i, i.e., the AMA index related to the variance of V_m, coincides with the principal Sobol' index S_i if the conditional variance, $V[V_m|P_i]$, is always (i.e., for each value of P_i) smaller than (or equal to) its unconditional counterpart $V(V_m)$.

As expected, Figure 7a reveals that conditioning V_m on the value of fracture aperture markedly affects the mean value of V_m, knowledge of m or $\Delta p/k$ being influential to a lesser extent. Conditioning on increasing m values leads to a decrease of the mean of V_m, the opposite trend being observed as a result of conditioning on w and $\Delta p/k$. These results are consistent with the conceptual and physical picture of the system behavior, i.e., mud losses increase when (a) the fracture aperture increases, (b) the shear stress decreases (i.e., m decreases) or (c) overpressure increases. The variance of V_m is strongly reduced (up to a factor of about 1/5 across the range of parameter variability explored) by conditioning on w values, and can be significantly larger than its unconditional counterpart by conditioning on low values of m or on large $\Delta p/k$ ratios (see Figure 7b). Knowledge of the fracture aperture does not significantly contribute to change the shape of the pdf of V_m, as rendered through the skewness and kurtosis coefficients depicted in Figures 7c and 7d, respectively. Otherwise, knowledge of m can significantly decrease the values of skewness and kurtosis, rendering the pdf of V_m nearly symmetric and platykurtic (i.e., with less extreme values than the Normal distribution). Notably, fixing τ_Y/k or r_w does not affect any of the first four moments of the pdf of V_m. Figure 8 complements Figure 7 by depicting the AMA indices obtained through (15). These graphs indicate that the uncertainty of the mean and variance of the pdf of V_m is primarily driven by the fracture aperture, followed by m and $\Delta p/k$. Otherwise, the shape of the pdf of V_m, the evaluation of which is key in the context of a risk assessment framework, is primarily affected by m, followed by $\Delta p/k$.

5. Stochastic inverse modeling

It is well known that model calibration outputs depend on the quality and quantity of available information and may vary depending on the inverse methodology employed. While a deterministic approach is geared towards finding a unique set of model parameters that minimizes a given objective function, stochastic calibration allows reconstructing the pdf of each (unknown) parameter on the basis of available data, i.e., the posterior parameter density.

Here, we present and discuss the results of three stochastic calibration strategies that we briefly describe (Section 5.1) and then apply (Section 5.2) to the model introduced in Section 2.

5.1 Stochastic Calibration Strategies

All stochastic calibration strategies here employed are grounded on the evaluation of the following function

$$F = \sum_{j=1}^{n_t}\left(V_m^*(t_j) - V_m(t_j)\right)^2, \tag{16}$$

where n_t is the number of available mud flow rate measurements, $V_m^*(t_j)$ is the total mud volume invading the fracture system at time t_j and detected as detailed in Section 3.1, $V_m(t_j)$ being its counterpart computed via (8).

The first two strategies we consider are based on the minimization of (16) via two diverse optimization techniques. Both techniques are computationally efficient and accurate in the context of non-linear inverse problems and do not require the evaluation of gradients of the objective function. The first method, hereafter termed NMS, is grounded on the widely applied Nelder-Mead Simplex approach (Lagarias et al. 1998), as implemented in the Matlab® environment (routine *fminsearch*). NMS relies on a simplex of (N+1) vertexes in an N-dimensional space (N being the number of unknown parameters). At each iteration, the algorithm evaluates (16) at each vertex of the simplex, discards the vertex with the largest value of the objective function (16) and replaces it with a new one. In our study we obtain stable results with 10^4 iterations. The second methodology is the Particle

361 Swarm Optimization (PSO) technique (Eberhart and Kennedy 1995, Robinson and Rahmat-Samii
362 2004). The latter is guided by the concept of swarm movement and intelligence. It is inspired by the
363 idea of a bees' flock seeking for the highest density of flowers, the entire swarm moving according
364 to information collected by each individual. PSO requires evaluating the model at a number of points,
365 N_p, in the parameter space which is much larger than the number of model parameters. A brief
366 description of the algorithm is included in Appendix B. We note that, due to the nature of these two
367 techniques, inverse modeling yields a collection of sets of model parameters satisfying an imposed
368 convergence criterion. These are then analyzed through their empirical frequency distributions. As
369 such, the ensuing results correspond to a frequentist analysis of a set of model parameter estimates.
370 The third methodology relies on Acceptance-Rejection Sampling (ARS). The latter is an
371 unbiased sampler and aims at generating multiple independent realizations of the model output by
372 sampling from the posterior parameter distribution conditioned on the observations. At each iteration,
373 a random set of model parameters are independently sampled within the support defined by the ranges
374 listed in Table 1, (16) is evaluated and the candidate parameter set is *accepted* or *rejected* by
375 considering threshold criteria based on the likelihood function. Details of the ARS are given in
376 Appendix C.
377
378 **5.2 Results**
379 Here, we present and compare some key results of the three stochastic calibration strategies
380 described above, as applied to the showcase setting illustrated in Section 3, and explore the benefit
381 of assisting stochastic calibration through GSA. We remark that stochastic calibrations are
382 computationally demanding and would not be feasible without resorting to (*a*) the analytical model
383 presented in Section 2 and (*b*) the assistance of the GSA illustrated in Section 4.
384 We start by noting that all calibration techniques yield results that are consistent with the
385 observations. As an example, Figure 9 depicts the temporal evolution of the drilling mud volume loss
386 data, V_m^*, for the four events described in Section 3 (symbols) as well as the analytical solution (8)

where parameter values correspond to selected realizations of V_m obtained from NMS-based calibrations (continuous curves). Results of similar quality have been obtained with all calibration strategies (not shown).

5.2.1 Stochastic model calibration *unassisted* by GSA

In this Section we analyze the sample pdfs of w and r_f obtained via the three stochastic calibration methodologies (NMS, PSO and ARS) and without considering the results of the GSA performed in Section 4. In the following we refer to this calibration as "*unassisted"* by GSA. Results are illustrated only for the two longest events, i.e., event 3 and 4 (see Figure 9). Similar outcomes have been obtained for the remaining events.

Figure 10 depicts the sample (posterior) pdfs of r_f and w computed with all calibration methods. Tables 2 and 3 summarize the main statistics for event 3 and 4, respectively. All calibration methods yield very similar mean values for w (as well as for r_f) and consistent with the kind of reservoir subject to our study (Galvis Barros 2018). Otherwise, the variance and the shape of the pdfs (as rendered also in terms of higher order moments) is influenced by the stochastic inverse method adopted.

Sample densities obtained for τ_Y/k, $\Delta p/k$, m and r_w are included in Appendix D (see Figure D1). Results obtained via ARS are close to the prior (i.e., uniform) distributions, revealing that mud loss measurements are not highly informative to the assessment of the values of these parameters. As discussed in Section 3, even as we treat these parameters as random quantities, their variability is restrained (and it is much smaller than the one displayed by w) because their value is estimated via laboratory measurements (for τ_Y, k, and m) or constantly monitored during drilling (for Δp and r_w). Otherwise, sample pdfs of parameters obtained via NMS and PSO differ from the prior pdfs.

As already discussed in Section 5.1, while NMS and PSO rely on (different) minimization algorithms, ARS is based on a sampling procedure. Note also that ARS requires a computational time that is much larger (i.e., of about 8 times, in our study) than the one needed for PSO or NMS.

5.4.2 Stochastic model calibration *assisted* by GSA

In the following we perform stochastic model calibration by taking into account GSA results (hereafter called "*assisted*" calibrations) presented in Section 4. Considering the ranges of parameter variability of Table 1, GSA suggests that the pdf of V_m is almost insensitive to the choice of τ_Y/k and r_w. The efficiency of stochastic model calibration could then be improved by fixing the values of these two model parameters.

Figure 11 depicts the (sample) posterior pdfs of w and r_f obtained with all calibration methods for events 3 and 4 upon fixing the values of τ_Y/k and r_w to the average of their corresponding range of variability, i.e., $\tau_Y/k = 7\ \mathrm{s}^{-m}$, and r_w = 0.1 m. The results obtained in Section 5.4.1 (*unassisted* calibration) are also depicted for comparison purposes. The first four statistical moments of the sample pdfs of w and r_f are listed in Tables 2 and 3 for event 3 and 4, respectively. Tables 2 and 3 also include values of the Kullback-Leibler divergence (D_{KL}) (Kullback 1959), which is a global measure employed to quantify the difference between the posterior pdfs obtained through the *unassisted* and *assisted* calibrations.

Assisted and *unassisted* ARS calibrations yield very similar parameter distributions (see Figures 11 a, b, g, h), as also quantified by the small values of D_{KL}. It is remarked that performing the *assisted* calibrations requires a significantly reduced computational time (of a factor of about 1/5 in our showcases) with respect to the *unassisted* ones without affecting the sample posterior pdf of the quantities of interest. These results suggest that relying on ARS (and NMS, albeit to a lesser extent) for stochastic model calibration would clearly benefit from a preliminary (moment-based) GSA analysis.

435 Otherwise, the *assisted* pdfs of w and r_f obtained via PSO exhibit a shape which is, in general,
436 different from their *unassisted* counterparts (albeit mean and variance do not change dramatically),
437 as shown by Fig. 11 (c-f, i-n) and quantified by D_{KL}. These results suggest that the use of PSO for
438 stochastic model calibration might not benefit from a preliminary GSA analysis.
439 Finally, we recall that our moment-based GSA recognizes m and/or $\Delta p/k$ as influential to the
440 pdf of V_m (see Figures 8c-d). Figure 12 confirms that setting these parameters to a given value
441 significantly changes the results of the stochastic model calibration. We remark that this important
442 finding would not have been detected by classical GSA analyses based on scatter plots or Sobol'
443 indices.
444
445 **6. Conclusions**
446 We analyze the way mud loss events can be used to characterize a fractured reservoir within
447 a stochastic inversion framework. We do so by formulating an original analysis framework which
448 merges two parallel streams of research, i.e., Global Sensitivity Analysis (GSA) and stochastic
449 inverse modeling. We rest on a simple analytical model to describe, in real-time and under uncertain
450 conditions, the aperture and extent of a fracture (or a set of fractures) encountered in a formation
451 while drilling. Our work leads to the following major conclusions.
452 1. The choice of the inversion method does not affect the stochastic calibration results in term
453 of the mean value of the ensuing posterior pdfs. Otherwise, it can affect the stochastic results
454 in terms of the higher order moments of the posterior pdf.
455 2. Results from our moment-based GSA suggest that uncertainty associated with m and/or
456 $\Delta p/k$ influence the pdf of the total mud volume lost (V_m) while drilling. A moment-based
457 GSA (relying on the AMA indices) can be employed as an efficient tool to assist stochastic
458 inverse modeling, yielding a notably reduced computational time, without affecting the
459 posterior pdf of the quantities of interest, when Acceptance Rejection Sampling (ARS) is
460 employed for the calibration. Conversely, a stochastic inverse modeling strategy relying on

a minimization algorithm such as Particle Swarm Optimization (PSO) might not benefit from a preliminary GSA.

3. When ARS is used jointly with the evaluation of the AMA indices, mud loss data can be efficiently employed to refine the real-time prediction (under uncertainty) of fracture aperture and extent. Otherwise, mud loss data appear to be uninformative to refine prior knowledge about mud rheological properties as well as overpressure and wellbore radius.

Appendix A: Derivation of the analytical model and theoretical analysis

The momentum equation (1) and the strain rate tensor, $\overline{\boldsymbol{\gamma}}$, in cylindrical coordinates read

$$\begin{cases} \rho\frac{dv_r}{dt} = -\frac{\partial p'}{\partial r} - \frac{\partial \tau_Y}{\partial r} - k\left[\frac{\partial \gamma_{rr}^m}{\partial r} + \frac{1}{r}\frac{\partial \gamma_{\theta r}^m}{\partial \theta} + \frac{\partial \gamma_{zr}^m}{\partial z} + \frac{1}{r}(\gamma_{rr}^m - \gamma_{\theta\theta}^m)\right] \\ \rho\frac{dv_\theta}{dt} = -\frac{1}{r}\frac{\partial p'}{\partial \theta} - \frac{1}{r}\frac{\partial \tau_Y}{\partial \theta} - k\left[\frac{\partial \gamma_{r\theta}^m}{\partial r} + \frac{1}{r}\frac{\partial \gamma_{\theta\theta}^m}{\partial \theta} + \frac{\partial \gamma_{z\theta}^m}{\partial z} + \frac{1}{r}(\gamma_{r\theta}^m + \gamma_{\theta r}^m)\right] \\ \rho\frac{dv_z}{dt} = -\rho g - \frac{\partial p'}{\partial z} - \frac{\partial \tau_Y}{\partial z} - k\left[\frac{\partial \gamma_{rz}^m}{\partial r} + \frac{1}{r}\frac{\partial \gamma_{\theta z}^m}{\partial \theta} + \frac{\partial \gamma_{zz}^m}{\partial z} + \frac{\gamma_{rz}^m}{r}\right] \end{cases} \quad \text{(A.1)}$$

$$\overline{\boldsymbol{\gamma}} = \begin{bmatrix} \frac{\partial v_r}{\partial r} & \frac{1}{2}\left(r\frac{\partial}{\partial r}\frac{v_\theta}{r} + \frac{1}{r}\frac{\partial v_r}{\partial \theta}\right) & \frac{1}{2}\left(\frac{\partial v_r}{\partial z} + \frac{\partial v_z}{\partial r}\right) \\ \frac{1}{2}\left(r\frac{\partial}{\partial r}\frac{v_\theta}{r} + \frac{1}{r}\frac{\partial v_r}{\partial \theta}\right) & \frac{1}{r}\frac{\partial v_\theta}{\partial \theta} + \frac{\partial v_r}{\partial r} & \frac{1}{2}\left(\frac{\partial v_\theta}{\partial z} + \frac{1}{r}\frac{\partial v_z}{\partial \theta}\right) \\ \frac{1}{2}\left(\frac{\partial v_r}{\partial z} + \frac{\partial v_z}{\partial r}\right) & \frac{1}{2}\left(\frac{\partial v_\theta}{\partial z} + \frac{1}{r}\frac{\partial v_z}{\partial \theta}\right) & \frac{\partial v_z}{\partial z} \end{bmatrix}. \quad \text{(A.2)}$$

Considering laminar flow (i.e., $v_\theta = v_z = 0$), the problem is axisymmetric (i.e., $\frac{\partial v_r}{\partial \theta} = \frac{\partial p'}{\partial \theta} =$ 0) and (A.1)-(A.2) reduce to

$$\begin{cases} \rho\left(\frac{\partial v_r}{\partial t} + v_r\frac{\partial v_r}{\partial r}\right) = -\frac{\partial p'}{\partial r} - k\left[\frac{1}{r}\frac{\partial (r\gamma_{rr}^m)}{\partial r} + \frac{\partial \gamma_{zr}^m}{\partial z} - \frac{\gamma_{\theta\theta}^m}{r}\right] \\ 0 = -\rho g - \frac{\partial p'}{\partial z} - k\left[\frac{\partial \gamma_{rz}^m}{\partial r} + \frac{\gamma_{rz}^m}{r}\right] \end{cases} \quad \text{(A.3)}$$

$$\overline{\boldsymbol{\gamma}} = \begin{bmatrix} \frac{\partial v_r}{\partial r} & 0 & \frac{1}{2}\frac{\partial v_r}{\partial z} \\ 0 & \frac{v_r}{r} & 0 \\ \frac{1}{2}\frac{\partial v_r}{\partial z} & 0 & 0 \end{bmatrix}. \quad \text{(A.4)}$$

Substituting (A.4) into (A.3) yields

$$\begin{cases} \rho\left(\frac{\partial v_r}{\partial t} + v_r\frac{\partial v_r}{\partial r}\right) = -\frac{\partial p'}{\partial r} - k\left[\frac{1}{r}\frac{\partial}{\partial r}\left(\frac{\partial r v_r}{\partial r}\right)^m + \frac{\partial}{\partial z}\left(\frac{\partial v_r}{\partial z}\right)^m - \frac{1}{r}\left(\frac{v_r}{r}\right)^m\right] \\ 0 = -\rho g - \frac{\partial p'}{\partial z} - k\left[\frac{\partial}{\partial r}\left(\frac{1}{2}\frac{\partial v_r}{\partial z}\right)^m + \frac{1}{r}\left(\frac{1}{2}\frac{\partial v_r}{\partial z}\right)^m\right] \end{cases}. \quad \text{(A.5)}$$

Making use of mass conservation, i.e., $(\partial(rv_r))/\partial r = 0$, considering that the viscous term is dominant over the inertial one, i.e., $\rho\frac{\partial v_r}{\partial t} \ll k\left[\frac{\partial}{\partial z}\left(\frac{\partial v_r}{\partial z}\right)^m\right]$, noting that $\left(\frac{\partial v_r}{\partial r} \ll \frac{\partial v_r}{\partial z}\right)$ and

$$\frac{\partial}{\partial r}\left(\frac{\partial v_r}{\partial z}\right)^m = m\left(\frac{\partial v_r}{\partial z}\right)^{m-1}\frac{\partial^2 v_r}{\partial r \partial z} = m\left(\frac{\partial v_r}{\partial z}\right)^{m-1}\frac{\partial}{\partial z}\left(-\frac{v_r}{r}\right) = -\frac{m}{r}\left(\frac{\partial v_r}{\partial z}\right)^m \quad \text{(A.6)}$$

and introducing the quantity $p = p' + \rho g$, (A.5) becomes

$$\begin{cases} \frac{\partial p}{\partial r} = -k\,\frac{\partial}{\partial z}\left[\left(\frac{\partial v_r}{\partial z}\right)^m\right] \\ \frac{\partial p}{\partial z} = -\frac{k}{r}\frac{(1-m)}{2^m}\left(\frac{\partial v_r}{\partial z}\right)^m \end{cases}. \tag{A.7}$$

Note that the vertical gradient of p (*i*) vanishes when $m = 1$ (i.e., for a Newtonian or Bingham plastic fluid) and (*ii*) decreases as the distance from the pumping well, r, increases. Therefore, pressure is hydrostatic when $m = 1$ or tends to become hydrostatic (for $m \neq 1$) as the distance from the well increases.

The mud flow rate, Q, can be obtained by integrating (7) along the fracture aperture, resulting in

$$Q = \pi r w^2 \left(\frac{m}{2m+1}\right)\left[-\frac{w}{2k}\frac{\partial p}{\partial r}\right]^{\frac{1}{m}}\left[1 + \frac{2}{w}\left(\frac{2m+1}{m+1}\right)\frac{\tau_Y}{\frac{\partial p}{\partial r}}\right]^{\frac{1}{m}}. \tag{A.8}$$

Evaluating Q^m from (A.8), expanding Q^m as a Taylor series in terms of $\tau_Y/(-\frac{w}{2}\frac{\partial p}{\partial r})$ and retaining only the first two terms in the expansion, yields the following approximate solution for the pressure gradient:

$$-\frac{\partial p}{\partial r} = \frac{2}{w}\left(\frac{kQ^m}{\left[\pi r \frac{m}{2m+1} w^2\right]^m} + \frac{2m+1}{m+1}\tau_Y\right). \tag{A.9}$$

A closed-form expression for $\Delta p = p_w - p_f$ can be obtained by integrating (A.9) from the wellbore radius, r_w (with pressure p_w), to the to the mud front r_f (with pressure p_f), as:

$$\Delta p = \frac{2}{w}\frac{k\,Q^m\left(r_f^{1-m} - r_w^{1-m}\right)}{(1-m)\left(\pi \frac{m}{2m+1}\, w^2\right)^m} + \frac{2m+1}{m+1}\frac{2\tau_Y}{w}(r_f - r_w). \tag{A.10}$$

Appendix B: Particle Swarm Optimization algorithm

We start by introducing the vector $\boldsymbol{x}$ of $N_p \times N$ entries. The optimal choice for the number of particles N_p to sample the N-dimensional parameter space (N = 5 in our example) is problem-dependent. The results included in Section 5 have been obtained with N_p = 50, similar findings being achieved with $40 \leq N_p \leq 80$.

PSO is implemented according to the following steps:

1. Step $i = 0$. Random selection of a number N_p of points $\boldsymbol{x}_0(j)$ with $j = 1, \ldots, N_p$ within the N-dimensional parameter space together with a random value of a displacement vector $\boldsymbol{v}_0(j)$.
2. Displace the N_p particles within the N-dimensional space as $\boldsymbol{x}_{i+1}(j) = \boldsymbol{x}_i(j) + \boldsymbol{v}_i(j)$.
3. Evaluate (16) and select the value of $j = j_{\text{best}}$ (i.e., the particle) giving the minimum of (16) and set $\boldsymbol{g}_{\text{best}} = \boldsymbol{x}_{\text{best}} = \boldsymbol{x}(j_{\text{best}})$.
4. Evaluate a new displacement $\boldsymbol{v}_{i+1}(j) = \omega\ \boldsymbol{v}_i(j) + c_1 U[\boldsymbol{x}_{\text{best}} - \boldsymbol{x}_i(j)] + c_2 U[\boldsymbol{g}_{\text{best}} - \boldsymbol{x}_i(j)]$ where U is a random number uniformly distributed between 0 and 1, c_1 and c_2 are constant coefficients and ω is a step dependent variable (Lagarias et al. 1998). Here, we follow Rahmat-Samii and Michielssen (1999) and fix $c_1 = c_2 = 1.495$.
5. Update the particle position with the displacement evaluated at step 4, evaluate (16), select the value of $j = j_{\text{best}}$ (i.e., the particle) rendering the minimum of (16) and set $\boldsymbol{x}_{\text{best}} = \boldsymbol{x}(j_{\text{best}})$. If (16) evaluated with $\boldsymbol{x}_{\text{best}}$ is smaller than (16) evaluated with $\boldsymbol{g}_{\text{best}}$, set $\boldsymbol{g}_{\text{best}} = \boldsymbol{x}_{\text{best}}$, otherwise set $\boldsymbol{g}_{\text{best}} = \boldsymbol{g}_{\text{best}}$.
6. Set $i = i + 1$ and go to Step 2.

Steps 2-6 are repeated until the maximum number of prescribed displacements is reached. We set this quantity to 60 in our application. In order to avoid selection of a local minimum, PSO has been performed upon varying the initial condition $\boldsymbol{x}_0$, for a total of 800 iterations.

Appendix C: Acceptance-Rejection sampling

The objective of the sampling algorithm ARS is to draw random samples from the posterior pdf of a parameter set collected in vector $\boldsymbol{P}$, $f_{\boldsymbol{P}|\boldsymbol{V}_m^*}$, given a vector of n_t observed values of $\boldsymbol{V}_m^*$. According to Bayes' theorem

$$f_{\boldsymbol{P}|\boldsymbol{V}_m^*} \propto f_{\boldsymbol{P}} f_{\boldsymbol{V}_m^*|\boldsymbol{P}} \tag{C.1}$$

where $f_{\boldsymbol{V}^*_{\boldsymbol{m}}|\boldsymbol{P}}$ is the likelihood function and $f_{\boldsymbol{P}}$ is the prior pdf of $\boldsymbol{P}$. We assume that $f_{\boldsymbol{V}^*_{\boldsymbol{m}}|\boldsymbol{P}}$ is multiGaussian, i.e.,

$$f_{\boldsymbol{V}^*_{\boldsymbol{m}}|\boldsymbol{P}} = \left(2\pi\,\sigma^2_{V_m}\right)^{-n_t/2} \exp\{-\frac{1}{2\sigma^2_{V_m}}[\boldsymbol{V}^*_{\boldsymbol{m}} - \boldsymbol{V}_{\boldsymbol{m}}(\boldsymbol{P})]^T\,[\boldsymbol{V}^*_{\boldsymbol{m}} - \boldsymbol{V}_{\boldsymbol{m}}(\boldsymbol{P})]\} \quad \text{(C.2)}$$

where σ_{V_m} is the standard deviation of the measurement errors (which we set to 0.01 and 0.1, for event 3 and 4, respectively, in our application example).

ARS can be used to draw samples from $f_{\boldsymbol{P}|\boldsymbol{V}^*_{\boldsymbol{m}}}$ according to the following iterative procedure:

1. Sample N values from a uniform distribution in the interval (0,1) to obtain normalized parameters.
2. Map normalized parameters onto $\boldsymbol{P}$.
3. Evaluate (8) to compute the temporal evolution of $\boldsymbol{V}_{\boldsymbol{m}}(\boldsymbol{P})$.
4. Evaluate α_i that is the acceptance probability of $\boldsymbol{P}$ as

$$\alpha_i = \frac{f_{\boldsymbol{V}^*_{\boldsymbol{m}}|\boldsymbol{P}}}{\max\{f_{\boldsymbol{V}^*_{\boldsymbol{m}}|\boldsymbol{P}}\}} = \exp\{-\frac{1}{2\sigma^2_{V_m}}[\boldsymbol{V}^*_{\boldsymbol{m}} - \boldsymbol{V}_{\boldsymbol{m}}(\boldsymbol{P})]^T\,[\boldsymbol{V}^*_{\boldsymbol{m}} - \boldsymbol{V}_{\boldsymbol{m}}(\boldsymbol{P})]\} \quad \text{(C.3)}$$

5. Draw a random value u from a uniform distribution in the interval (0,1).
6. Accept current realization of $\boldsymbol{P}$ if $\ln(u) < \ln(\alpha_i)$, otherwise reject it and return to Step 1.

Steps 1-6 are repeated until a stable $f_{\boldsymbol{V}^*_{\boldsymbol{m}}|\boldsymbol{P}}$ is obtained. In our application, convergence has been attained after about 10^6 iterations.

Appendix D: Posterior probability distribution of model parameters resulting from stochastic inverse modeling

Acknowledgements

The Authors acknowledge funding from Geolog Srl (Project: *Feedback between mud losses and fractures during along wellbores in fractured formations*).

Conflict of interest

The authors declare no conflict of interest in preparing this article.

References

Al-Adwani T, Singh S, Khan B, Dashti J, Ferroni G, Martocchia A (2012, June 4-7) Real Time Advanced Surface Flow Analysis for Detection of Open Fractures. EAGE Annual Conference & Exhibition incorporating SPE Europec https://doi.org/10.2118/154927-MS

Alcolea A, Carrera J, Medina A (2006) Pilot points method incorporating prior information for solving the groundwater flow inverse problem. Adv Water Resour 29:1678–1689. doi:10.1016/j.advwatres.2005.12.009

ANSYS Inc.:ANSYS® FLUENT® User's guide, Rel. 12.1 (2009)

API draft, A. P. (2009) Rheology and hydraulics of oil-well Draft. In API Recommended Practice 13D Draft (p.16)

Campolongo F, Cariboni J, Saltelli A (2007) An effective screening design for sensitivity analysis of large models. Environ Model Softw 22:1509-1518 https://doi.org/10.1016/j.envsoft.2006.10.004

577 Carrera J, Neuman SP (1986) Estimation of aquifer parameters under transient and steady state
578 conditions: 2. Uniqueness, stability, and solution algorithms. Water Resour Res 22(2):211–27.
579 http://dx.doi.org/10.1029/ WR022i002p00211
580 Carrera J, Alcolea A, Medina A, Hidalgo J, Slooten LJ (2005) Inverse problem in hydrogeology.
581 Hydrogeol J,13(1):206–22. http://dx.doi.org/10.1007/ s10040-004-0404-7
582
583 Chen M, Izady A, Abdalla OA, Amerjeed M (2018) A surrogate-based sensitivity quantification and
584 Bayesian inversion of a regional groundwater flow model. J Hydrol 557:826-837.
585 https://doi.org/10.1016/j.jhydrol.2017.12.071
586
587 Dell'Oca A, Riva M, Guadagnini A (2017) Moment-based metrics for global sensitivity analysis of
588 hydrological systems. Hydrol Earth Syst Sci, 21:1-16. https://doi.org/10.5194/hess-21-6219-2017
589
590 Kennedy J and Eberhart R (1995) Particle Swarm Optimization. Proceedings of the IEEE
591 International Conference on Neural Networks, 4, 1942-1948.
592 http://dx.doi.org/10.1109/ICNN.1995.488968
593
594 Faysal A, Shahriar M, Sheikh Z I (2019) Computational fluid dynamics study of yield power law
595 drilling fluid flow through smooth-walled fractures. Journal of Petroleum Exploration and Production
596 Technology. https://doi.org/10.1007/s13202-019-0646-5
597
598 Galvis Barros N E (2018) Geomechanics, Fluid Dynamics and Well Testing, Applied to Naturally
599 Fractured Carbonate Reservoirs, Extreme Naturally Fractured Reservoirs. Springer Theses, Springer
600 International Publishing AG, part of Springer Nature. https://doi.org/10.1007/978-3-319-77501-2
601
602 Keller JB (1976) Inverse problems. Am. Math. Mon., 83:107–118

Kullback S (1959) Information Theory and Statistics. John Wiley, New York

Lagarias JC, Reeds JA, Wright MH, Wright PE (1998) Convergence Properties of the Nelder−Mead Simplex Method in Low Dimensions. SIAM Journal of Optimization, 9(1):112−147. doi:10.1137/S1052623496303470

Laloy E, Rogiers B, Vrugt JA, Mallants D, Jacques D (2013) Efficient posterior exploration of a high-dimensional groundwater model from two-stage Markov chain Monte Carlo simulation and polynomial chaos expansion. Water Resour Res 49:2664-82. doi:10.1002/wrcr.20226

Lavrov A (2014) Radial flow of non-Newtonian power-law fluid in a rough-walled fracture: effect of fluid rheology. Transp Porous Med (2014) 105(3):559-570. https://doi.org/10.1007/s11242-014-0384-6

Majidi R, Miska SZ, Ahmed R, Yu M, Thompson LG (2010) Radial flow of yield-power-law fluids: Numerical analysis, experimental study and the application for drilling fluid losses in fractured formations. J Petroleum Sci and Eng, 70(3):334-343, ISSN 920-4105. http://dx.doi.org/10.1016/j.petrol.2009.12.005

Majidi R, Miska SZ (2011) Fingerprint of Mud Losses into Natural or induced Fractures. SPE 143854 SPE European Formation Damage Conference held in Noordwijk, The Netherlands, 7–10 June 2011

Mara TA, Fajraoui N, Guadagnini A, Younes A (2017) Dimensionality reduction for efficient Bayesian estimation of groundwater flow in strongly heterogeneous aquifers, Stoch Environ Res Risk Assess 31:2313–26. doi 10.1007/s00477-016-1344-1

629

630 Medina A, Carrera J (1996) Coupled estimation of flow and solute transport parameters. Water
631 Resour Res 32(10):3063–76. http://dx.doi.org/ 10.1029/96WR00754

632

633 Mitsoulis E, Abdali SS (1993) Flow Simulation of Herschel-Bulkley fluids through extrusion dies.
634 Can J Chem Eng 71:147-160. doi: 10.1002/cjce.5450710120

635

636 Neuman SP (1973) Calibration of groundwater flow models viewed as a multiple-objective decision
637 process under uncertainty. Water Resour Res 9(4):1006-21. http://dx.doi.org/10.1029/
638 WR009i004p01006

639

640 Pianosi F, Beven K, Freer J, Hall JW, Rougier J, Stephenson DB, Wagener T (2016) Sensitivity
641 analysis of environmental models: A systematic review with practical workflow. Environ Modell
642 Softw 79:214-232. https://doi.org/10.1016/j.envsoft.2016.02.008

643

644 Ratto M, Tarantola S, Saltelli A (2001) Sensitivity analysis in model calibration: GSA-GLUE
645 approach. Comput Phys Commun 136:212-224. 10.1016/S0010-4655(01)00159-X.

646

647 Razavi S, Gupta HV (2015) What do we mean by sensitivity analysis? The need for comprehensive
648 characterization of ‘‘global’’ sensitivity in Earth and Environmental systems models. Water Resour
649 Res 51:3070-92. https://doi.org/10.1002/2014WR016527

650

651 Razavi O, Lee HP, Olson JE, Schultz RA (2017) Drilling mud loss in naturally fractured reservoirs:
652 Theoretical modelling and field data analysis. SPE-187265-MS. https://doi.org/10.2118/187265-MS

653

654 Rehm B, Haghshenas A, Paknejad AS, Al-Yami A, Hughes J, Shubert J (2012) Underbalanced
655 drilling: Limits and extremes. Gulf Publishing Company, Houston, Texas
656
657 Robinson J, Rahmat-Samii Y (2004) Particle Swarm Optimization in Electromagnetics, IEEE
658 Transaction on antennas and propagation 52(2):397-407. doi: 10.1109/TAP.2004.823969
659
660 Roehl P, Choquette P (1985) Carbonate Petroleum Reservoir. New York City: Springer-Verlag
661
662 Russo E, Colombo I, Nicolotti I (2018) Uncertainty quantification of fracture characterization in
663 naturally fractured reservoirs. Presented at: FRONTUQ18 Pavia, Italy
664
665 Saltelli A, Ratto M, Andres T, Campolongo F, Cariboni J, Gatelli D (2008) Global sensitivity
666 analysis: The primer. Chichester, UK: John Wiley & Sons
667
668 Sobol I (1993) Sensitivity analysis for non-linear mathematical models. MMCE (Engl. Transl.) 1(4):
669 407-414. doi:1061-7590/93/04407-008
670
671 Sochala P, Le Maître OP (2013) Polynomial chaos expansion for subsurface flows with uncertain soil
672 parameters. Adv Water Resour 62:139-154. https://dx.doi.org/10.1016/j.advwatres.2013.10.003
673
674 Song X, Zhang J, Zhan C, Xuan Y, Ye M, Xu C (2015) Global sensitivity analysis in hydrological
675 modeling: Review of concepts, methods, theoretical framework, and applications, J Hydrol 523:739-
676 757. https://doi.org/10.1016/j.jhydrol.2015.02.013
677

678 Sudret B, Marelli S, Wiart J (2017) Surrogate models for uncertainty quantification: An overview.
679 11th European Conference on Antennas and Propagation (EUCAP), Paris, 2017, pp. 793-797.
680 doi: 10.23919/EuCAP.2017.7928679
681
682 Tang J, Zhuang Q (2009) A global sensitivity analysis and Bayesian inference framework for
683 improving the parameter estimation and prediction of a process-based Terrestrial Ecosystem
684 Model. J Geophys Res, 114, D15303. doi: 10.1029/2009JD011724
685
686 Van Griensven A, Meixner T, Grunwald S, Bishop T, Diluzio M, Srinivasan R (2006) A global
687 sensitivity analysis tool for the parameters of multi-variable catchment models. J Hydrol 324:10-23.
688 https://doi.org/10.1016/j.jhydrol.2005.09.008
689
690 World Energy Outlook (2006) International Energy Agency
691
692 Zhou H, Gómez-Hernández JJ, Li L (2014) Inverse methods in hydrogeology: Evolution and recent
693 trends. Adv Water Resour 63:22-37. doi:10.1016/j.advwatres.2005.12.009

	w [m]	τ_Y [Pa]	k [Pa s^m]	m	Δp [10^6 Pa]	r_w [m]
Min	5.0×10^{-5}	4.08	0.614	0.50	2.5	0.10
Max	1.0×10^{-2}	5.10	0.900	0.60	3.0	0.15

Table 1 Range of variability of model parameters

		Mean [m]	Variance [m^2]	Skewness	Kurtosis	D_{KL}
w	ARS *unassisted*	4.34×10^{-4}	1.88×10^{-9}	0.22	2.82	0.022
	ARS *assisted*	4.46×10^{-4}	2.64×10^{-9}	0.14	2.46	
	PSO *unassisted*	4.69×10^{-4}	1.56×10^{-9}	0.53	2.39	0.135
	PSO *assisted*	4.50×10^{-4}	0.61×10^{-9}	0.95	4.08	
	NMS *unassisted*	4.68×10^{-4}	2.41×10^{-9}	-0.10	2.62	0.025
	NMS *assisted*	4.70×10^{-4}	2.28×10^{-9}	0.04	2.58	
r_f	ARS *unassisted*	9.81	0.326	0.25	2.50	0.012
	ARS *assisted*	9.76	0.293	0.21	2.48	
	PSO *unassisted*	9.55	0.154	-0.33	2.19	0.462
	PSO *assisted*	9.74	0.077	-0.49	3.88	
	NMS *unassisted*	9.56	0.243	0.42	3.00	0.015
	NMS *assisted*	9.56	0.225	0.22	2.81	

Table 2 First four statistical moments of the pdfs of w and r_f for event 3 computed with all three stochastic calibration methods analyzed. Values of the Kullback-Leibler divergence (D_{KL}), quantifying the difference between (sample) posterior pdfs obtained via the *unassisted* and *assisted* calibrations are also listed.

		Mean [m]	Variance [m^2]	Skewness	Kurtosis	D_{KL}
w	ARS *unassisted*	4.74×10^{-4}	2.94×10^{-9}	0.203	2.50	0.006
	ARS *assisted*	4.79×10^{-4}	2.99×10^{-9}	0.240	2.46	
	PSO *unassisted*	4.46×10^{-4}	1.30×10^{-9}	0.071	2.09	0.213
	PSO *assisted*	4.36×10^{-4}	6.29×10^{-9}	-0.327	2.81	
	NMS *unassisted*	4.83×10^{-4}	3.07×10^{-9}	0.073	2.51	0.094
	NMS *assisted*	4.82×10^{-4}	3.06×10^{-9}	-0.050	2.60	
r_f	ARS *unassisted*	16.71	0.856	0.144	2.54	0.031
	ARS *assisted*	16.63	0.836	0.136	2.50	
	PSO *unassisted*	17.04	0.486	0.208	2.58	0.347
	PSO *assisted*	17.24	0.297	0.463	5.32	
	NMS *unassisted*	16.55	0.814	0.326	2.53	0.086
	NMS *assisted*	16.60	0.830	0.426	2.64	

Table 3 First four statistical moments of the pdfs of w and r_f for event 4 computed with all three calibration methods analyzed. Values of the Kullback-Leibler divergence (D_{KL}), quantifying the difference between (sample) posterior pdfs obtained via the *unassisted* and *assisted* calibrations are also listed

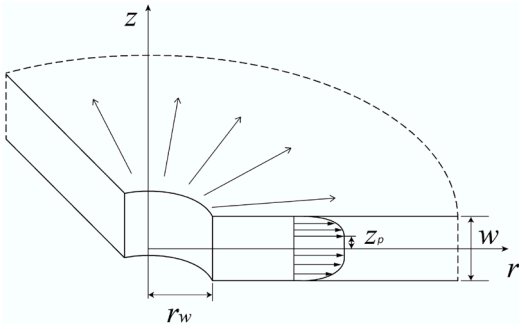

Fig. 1 Scheme of the problem setting and velocity profile of a Herschel-Bulkley fluid

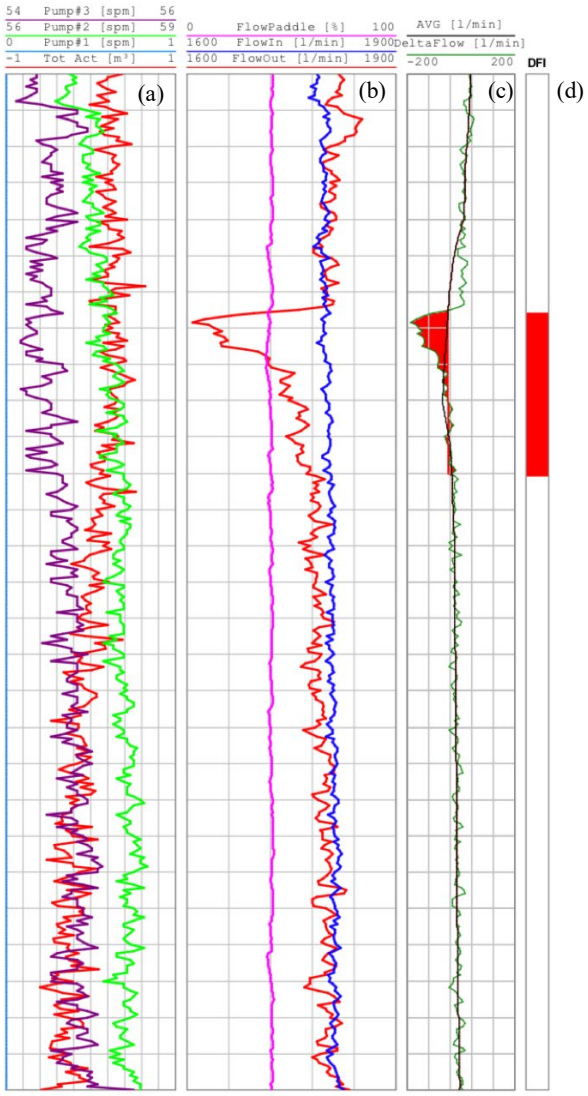

Fig. 2 Example of temporal data streams acquired while drilling. Temporal evolution of (a) SPM (strokes per minutes) for 3 pumps, and total active volume of mud (m^3); (b) flow-in, Q_{in} (l/min), flow-out, Q_{out} (l/min), and flow paddle (%); (c) delta flow, i.e. $\Delta Q = Q_{out} - Q_{in}$ (l/min); (d) Open fracture detection through real time drilling parameters and delta flow interpretation (DFI). Data are related to event 4

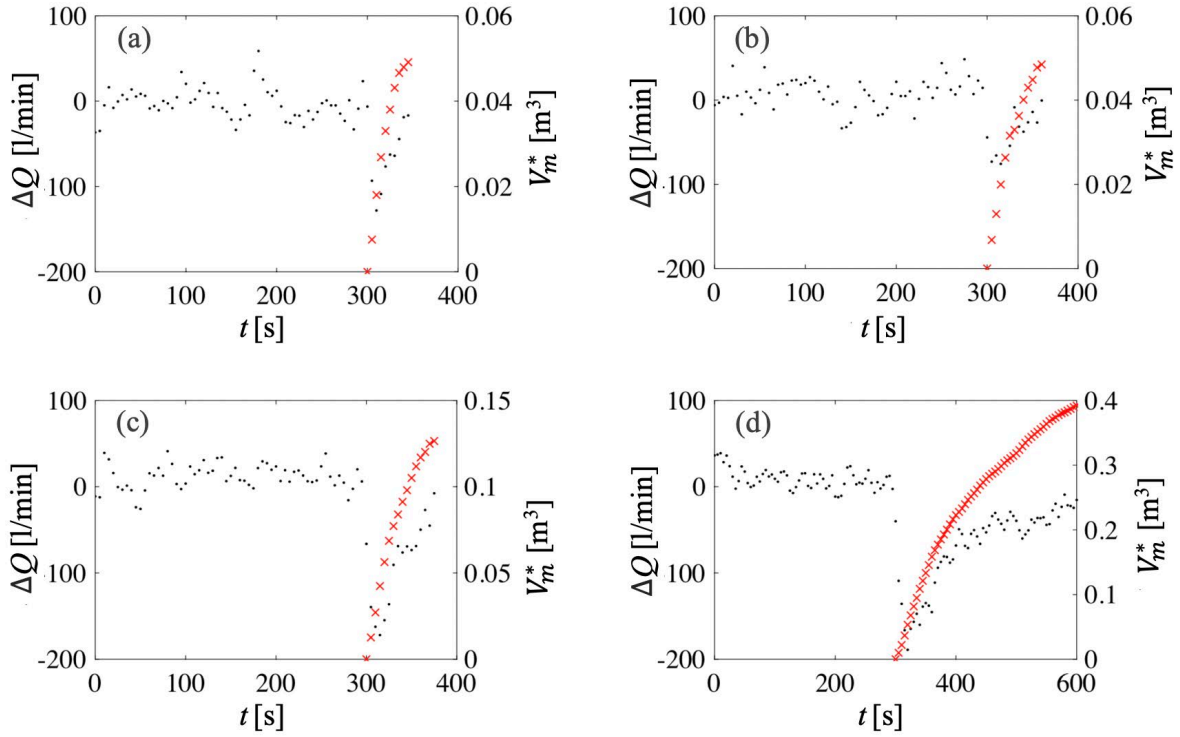

Fig. 3 Temporal evolution of ΔQ (black symbols) and V_m^* (red crosses) measured at a well during drilling. Each panel corresponds to the detection of a fracture (or of a fracture system), as suggested by the temporal behavior of ΔQ and corresponding to mud loss event (a) 1, (b) 2, (c) 3, and (d) 4

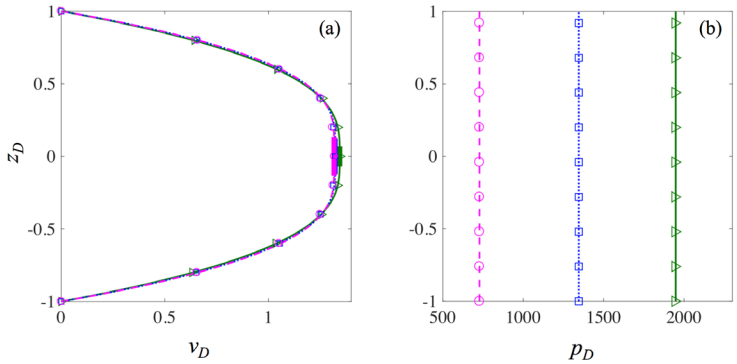

Fig. 4 Analytical (curves) and numerical (symbols) dimensionless vertical profiles of (a) velocity and (b) overpressure at r_D = 500 (pink), 400 (blue), and 100 (green) evaluated by setting r_w/w = 0.1, r_f/w = 0.6, w = 1 mm, Q = 3.33×10^{-4} m^3/s (20 l/min), τ_Y = 4.15 Pa, m = 0.582, k = 0.632 Pa s^m

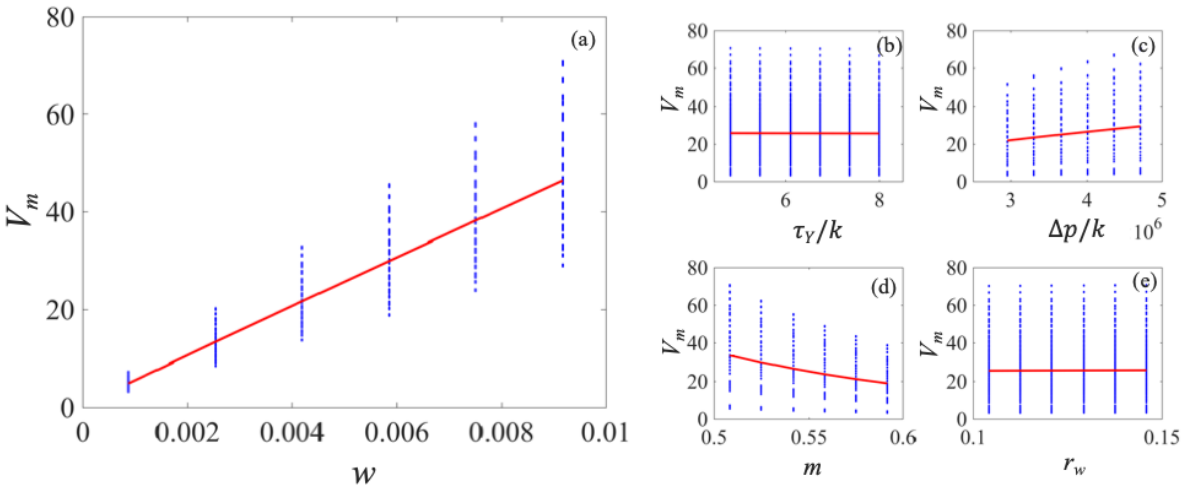

Fig. 5 Scatter plot of V_m (blue symbols) versus (a) w, (b) τ_Y/k , (c) $\Delta p/k$, (d) m, or (e) r_w. Red curves evidence the trend displayed by the clouds of points

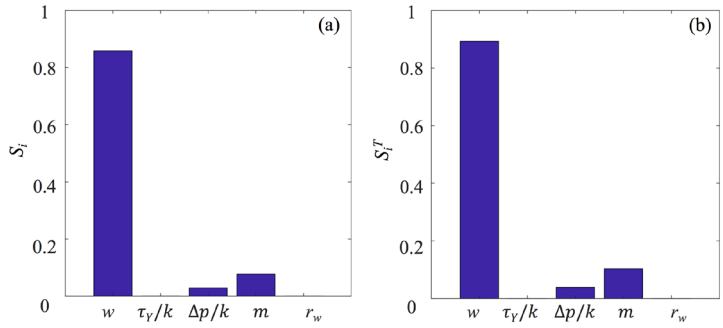

Fig. 6 (a) First order and (b) total Sobol' indices for each uncertain parameter $P_i = w$, τ_Y/k, $\Delta p/k$, m, or r_w

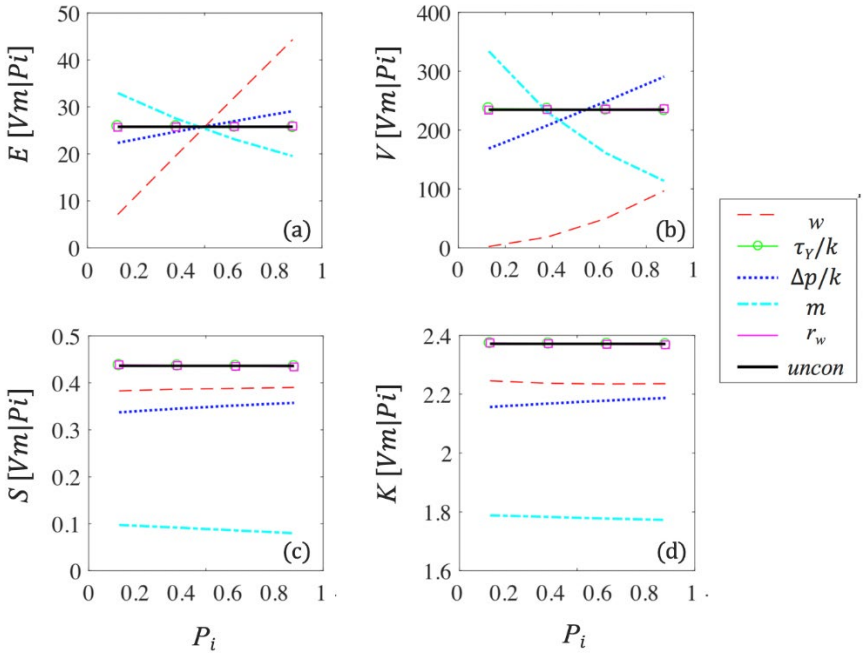

Fig. 7 Variation of the first four (statistical) moments of V_m as a function of values of $P_i = w$, τ_Y/k, $\Delta p/k$, m, or r_w: (*a*) expected value, (*b*) variance, (*c*) skewness, and (*d*) kurtosis. The corresponding unconditional moments are also depicted (black solid lines). Intervals of variation of each P_i are rescaled to span the range (0, 1) for graphical representation purposes

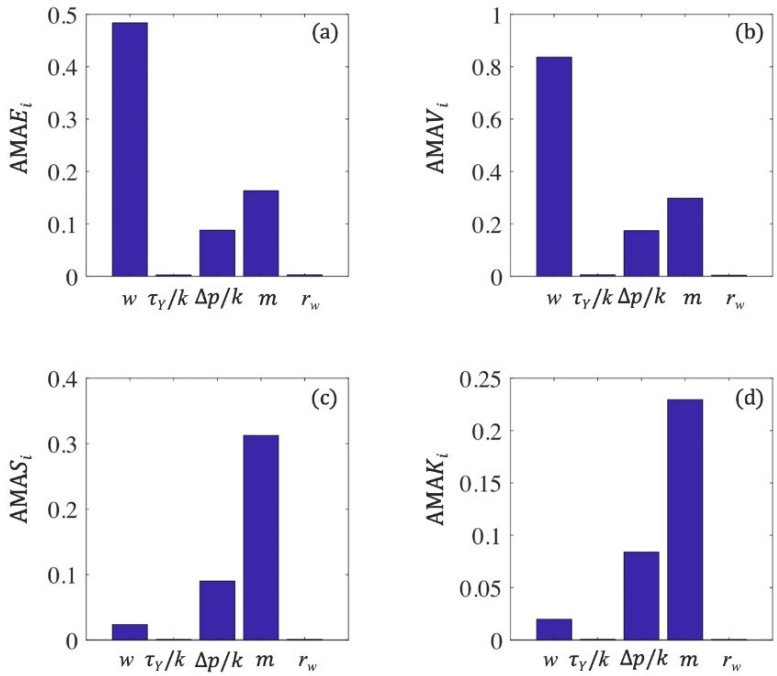

Fig. 8 Moment-based global sensitivity indices (defined as in (15)) associated with the (*a*) mean, (*b*) variance, (*c*) skewness, and (*d*) kurtosis of V_m

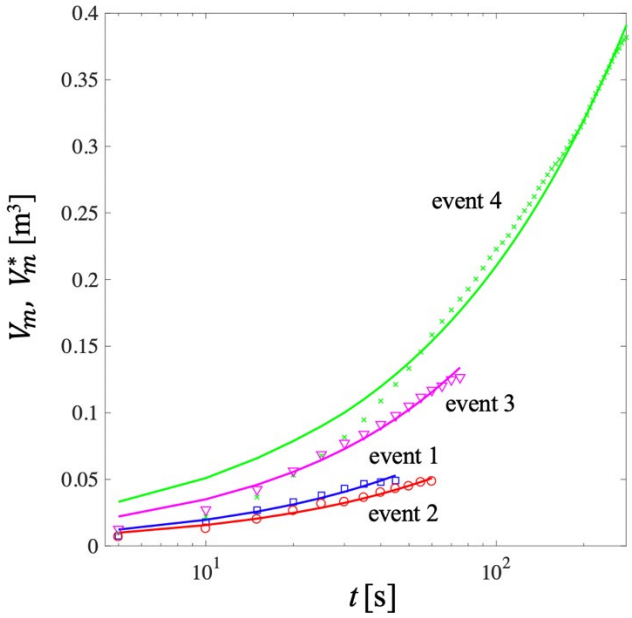

Fig.9 Temporal evolution of drilling mud volume loss V_m^* (symbols) and an example of outcomes of models calibrated via NMS, V_m, (continuous curves) for each event

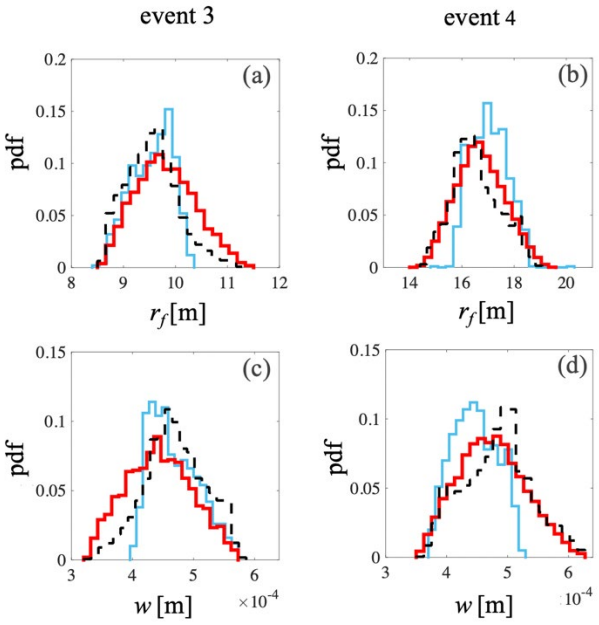

Fig. 10 Sample pdfs of r_f and w for event (a, c) 3 and (b, d) 4 obtained by stochastic *unassisted* inverse modeling implemented through NMS (black dashed curves), PSO (blues curves) and ARS (red curves)

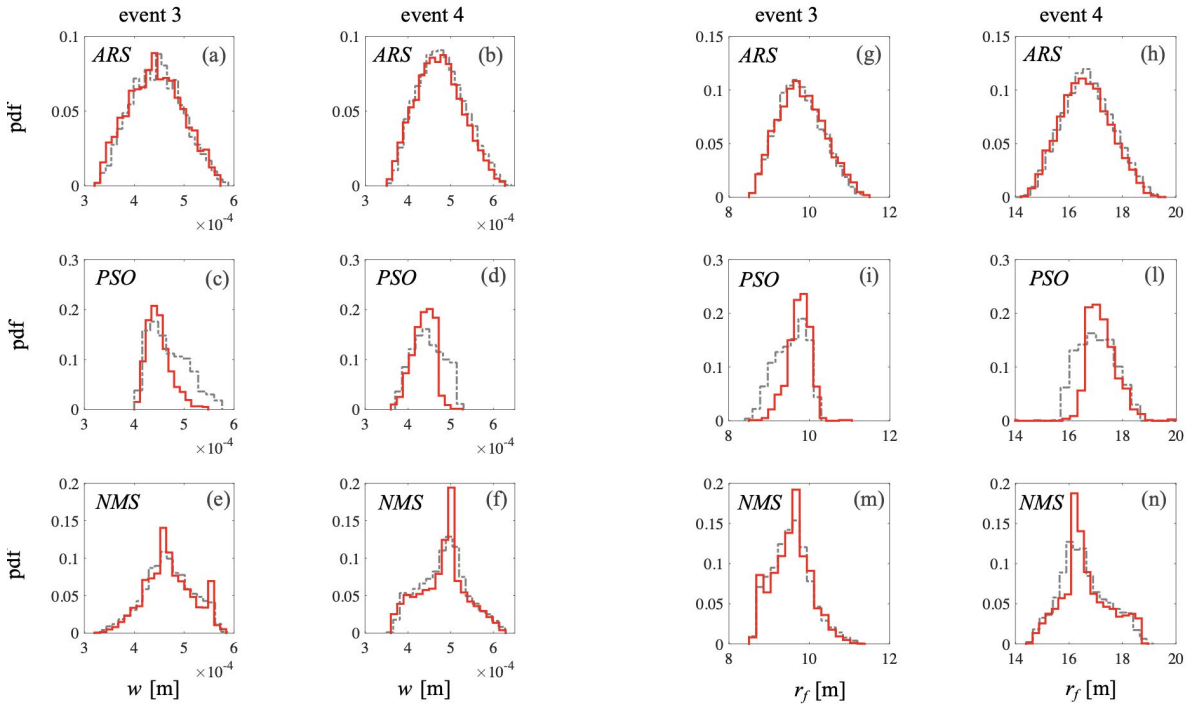

Fig. 11 Sample pdfs of w and r_f for events 3 and 4 obtained for *assisted* (red) and *unassisted* (grey dashed) stochastic inverse modeling through (a, b, g, h) ARS, (c, d, i, l) PSO, and (e, f, m, n) NMS. *Assisted* calibration is performed by setting $\tau_Y/k = 7\ \mathrm{s}^{-m}$ and $r_w = 0.1$ m

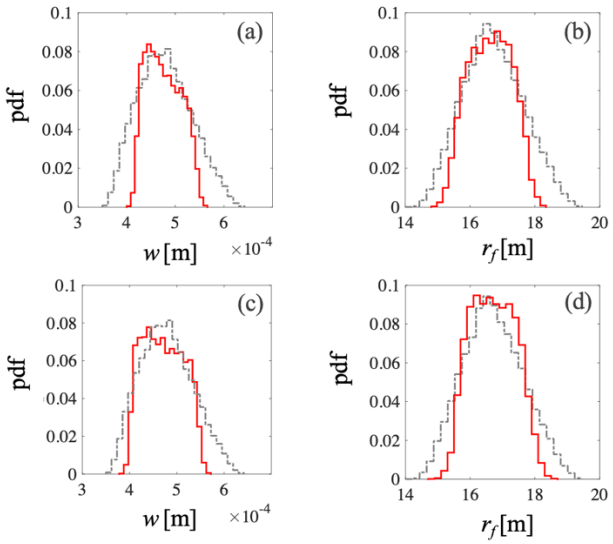

Fig. 12 Sample posterior pdfs of w and r_f for event 4 obtained for *assisted* (red) and *unassisted* (grey dashed) stochastic inverse modeling through the ARS method. *Assisted* calibration is performed by setting $\tau_Y/k = 7\ \mathrm{s}^{-m}$, r_w=0.1 m and (a)-(b) m = 0.55 and (c-d) $\Delta p/k = 3.83 \times 10^6\ \mathrm{s}^{-m}$

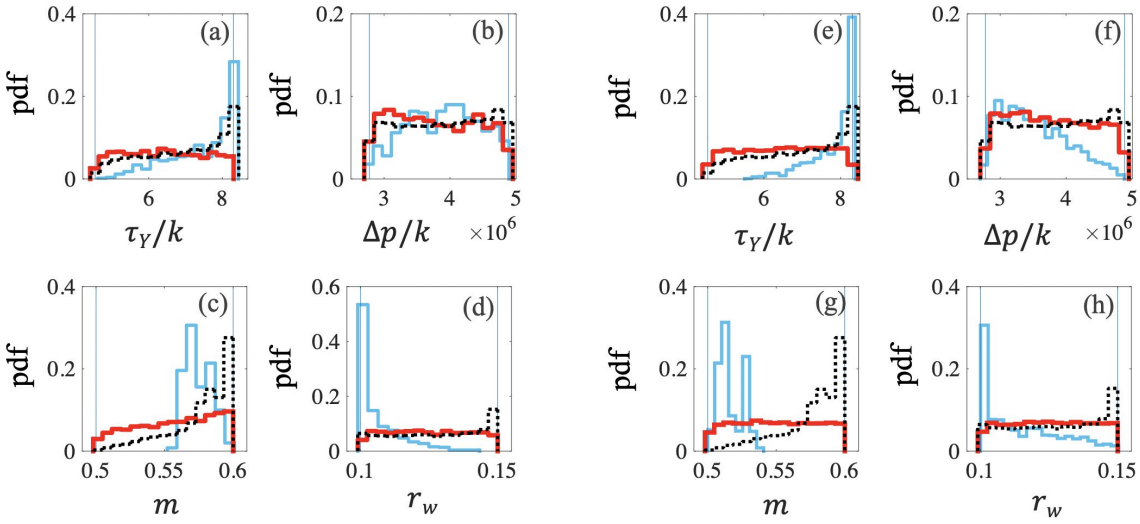

Fig. D1 Sample pdfs of τ_Y/k (a, e), $\Delta p/k$ (b, f), m (c, g) and r_w (d, h) obtained for event (a, b, c, d) 3 and (e, f, g, h) 4 by stochastic inverse modeling implemented via NMS (black dotted curves), PSO (blue curves) and ARS (red curves). Widths of the prior support have been computed from of experimental measurements taking into account measurements errors and relative error propagations